

Classification of retinal diseases based on OCT Images

Nabila Eladawi^{1,3}, Mohammed Elmogy^{2,3}, Mohammed Ghazal⁴, Omar Helmy⁵, Ahmed Aboelfetouh¹, Alaa Riad¹, Shlomit Schaal⁵, Ayman El-Baz³

¹Information Systems Department, Faculty of Computers and Information, Mansoura University, Egypt,

²Information Technology Department, Faculty of Computers and Information, Mansoura University, Egypt,

³Bioengineering Department, University of Louisville, Louisville, KY, USA, ⁴Electrical and Computer Engineering Department, Abu Dhabi University, Abu Dhabi, UAE, ⁵Department of Ophthalmology & Visual Sciences, University of Massachusetts Medical School, Worcester, MA, USA

TABLE OF CONTENTS

1. Abstract
2. Introduction
 - 2.1. Retina Anatomy in OCT
3. Related Work
 - 3.1. Normal healthy eye
 - 3.2. Glaucoma
 - 3.3. Central serous chorioretinopathy (CSC)
 - 3.4. Unilateral anterior ischemic optical neuropathy (AION)
 - 3.5. Diabetic macular edema (DME)
 - 3.6. Cystoids macular edema (CME)
 - 3.7. Age-related macular degeneration (AMD)
 - 3.8. Other different diseases
4. Challenges and future directions
 - 4.1. Automatic segmentation techniques
 - 4.2. OCT CAD systems
 - 4.3. Standard number of layers
 - 4.4. Weak layer boundaries
 - 4.5. Artifacts
5. Conclusion
6. Acknowledgment
7. References

1. ABSTRACT

Optical Coherence Tomography (OCT) is an emerging biomedical imaging technology that offers non-invasive real-time, high-resolution imaging of highly scattering tissues. It is widely used in ophthalmology to perform diagnostic imaging on the structure of the anterior eye and the retina. Clinical studies are carried out to assess the application of OCT for some retinal diseases. OCT can provide means for early detection for various types of diseases because morphological changes often occur before the physical symptoms of these diseases. In addition, follow-up imaging can assess treatment effectiveness and recurrence of a disease. A review in this area is needed to identify the results and the findings from OCT images in the field of retinal diseases and how to use these findings to help in

clinical applications. This paper overviews the current techniques that are developed to determine the ability of OCT images for early detection/diagnosis of retinal diseases. Also, the paper remarks several challenges that face the researchers in the analysis of the OCT retinal images.

2. INTRODUCTION

Optical Coherence Tomography (OCT) is one of the fastest developing medical imaging modalities in the last decade. It can capture different aspects of biological tissues, such as blood flow, polarization status, structure data, elastic parameters, and molecular content (1). Using OCT can give us accurate

knowledge of optical scattering and absorption of biological tissues. It helps in some diagnostic measurements, such as diagnosis of oral epithelial dysplasia, molecular diffusion in epithelial tissues, blood oxygenation measurement, blood glucose monitoring, plaque detection, and cancer detection (2, 3). Therefore, OCT can be used to diagnose different diseases by analyzing the change in human tissues in the captured images.

OCT is considered as non-invasive, fast, and single-cell resolution imaging through several millimeters of the biological tissues. OCT is the same as ultrasound imaging except for reflections of near-infrared light that are detected rather than sound. It uses infrared light to give high-resolution 3D insight into living tissues (4). It is based on low coherence interferometry to generate 2D and 3D images. This principle obtains high-resolution, cross-sectional, and backscattering profiles (5). Therefore, this imaging modality became popular due to ease of use, low cost, patient comfort, lack of ionizing radiation, and high resolution (6).

The first generation of OCT was time-domain OCT (TD-OCT). It encodes the location by time information about the position of a moving reference mirror to the location of the reflection. It can acquire up to 400 A-scans (Axial Scan) per second. In 2001, the spectral-domain OCT (SD-OCT) was invented. It can acquire all the information in a single A-Scan by evaluating the frequency spectrum of the interference between the reflected light and the reference mirror. SD-OCT is 40 to 110 times faster than TD-OCT. For example, Swept Source OCT is capable of acquiring 100000 A-scans per second, which allows 3D data collection (7). Recently, OCT has integrated with different imaging technologies, such as photoacoustics, multi-photon microscopy, fluorescent imaging, ultrasound, and adaptive optics, to overcome some of its limitations in order to enhance the performance (8).

OCT has been clinically used in ophthalmology (9, 10), cardiology (11, 12), endoscopy (13, 14), dermatology (15, 16) and oncology (15, 16). In developmental biology, OCT has been used to characterize the morphological and functional development of organs, such as eyes (17), brain (18), limbs (19), reproductive organs (20), and the heart (11, 18, 21, 22).

Moreover, OCT can be used for analysis of skin surface topography especially with the existence of high-definition OCT (HD-OCT). HD-OCT provides resolution of 3 μ m in both axial and “en-face” planes. It has fast acquisition time (2–3 seconds) (23). It provides non-invasive imaging of sub-surface skin tissues for screening skin diseases, such as basal cell carcinoma and inflammatory diseases (24). It can also be used

for fingerprint acquisition as it is capable of providing high-resolution 3D scans of the fingerprint skin, which contains much information about the fingerprint (25). In addition, OCT can help to understand some of the pathways influenced by the cardiac function in early heart development, such as the rapid beating and the complex ultrafine vasculature (26), coronary artery disease (27), and the structure of blood vessel wall in high details (28). On the other hand, OCT can be used to study brain diseases, such as brain tumors (29) and stroke (30). The high-resolution extension of OCT, optical coherence microscopy (OCM) (31, 32), can achieve 1–2 μ m resolution in tissue in all three dimensions. OCM can resolve individual neurons based on the intrinsic optical contrast in rodent brains (33, 34, 35) and human brain slices (36, 37).

As demonstrated in the literature, OCT shows promising results for diagnosing retinal diseases, which motivated us to focus on retina diseases in this short review. OCT can be considered as a standard modality for imaging the retina. Figure 1 shows an example of OCT retinal image for a typical normal person. OCT is a non-invasive scan of the retina that shows its cross-sectional profile. In other words, OCT is a high-resolution cross-sectional image of the layers of the eye's biological tissues. It is used to visualize the retina to recognize and assess a variety of ocular diseases, such as diabetic macular edema (DME), glaucoma, and age-related macular degeneration (AMD) (38, 39). The morphological features, such as the shape and distribution of drusen, cysts, macular holes, and blood vessels, can be easily visualized from OCT images and can be used as markers for diseases. Therefore, processing of OCT images becomes essential to do large scale studies for changes in retina's layers. Many of the used techniques rely on the consistency of the OCT layer intensities to provide accurate results (40).

2.1. Retina Anatomy in OCT

As it appears on OCT, the retina contains several layers with different thicknesses and intensities. Segmenting and measuring the thickness of each layer are considered as essential markers in assessing the health of the retina. The width and shape of individual layers may thicken or thin over the course of different diseases that indicate the current progress or status of a disease (40). Irregularities in images can be used to diagnose many retinal diseases, such as AMD, retinitis pigmentosa (RP), achromatopsia, glaucoma, and cone-rod dystrophy (CRD). The absence of certain layer(s) in the retina can be used as a marker for diagnosis, disease progression, and treatment monitoring (41).

Some studies preferred to define all intraretinal layer, whereas other studies preferred only to define the most critical retina layers that are needed

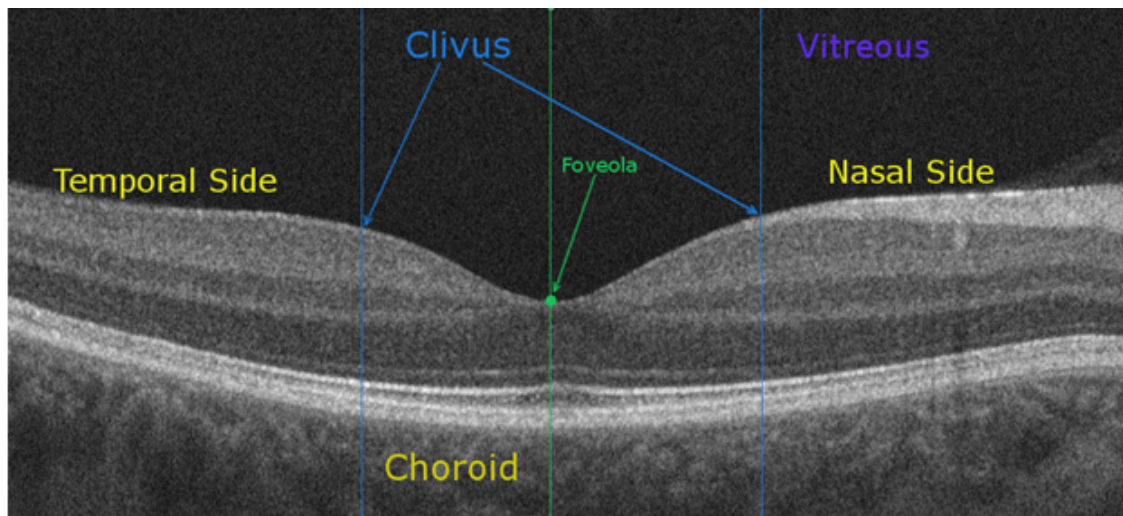


Figure 1. OCT retinal image for a typical normal person in macular region of retina.

to identify a disease. For example, Ishikawa *et al.* (42) defined four main layers, which are Nerve Fiber Layer (NFL), Ganglion Cell Layer (GCL) + Inner Plexiform Layer (IPL), Outer Plexiform Layer (OPL), and Outer Nuclear Layer (ONL) + Photoreceptor Layer for healthy and glaucomatous eyes. Garvin *et al.* (43) detected five various layers from 3D OCT images for a patient with unilateral Anterior Ischemic Optic Neuropathy (AION) disease. These five layers were NFL, GCL + IPL, Inner Nuclear Layer (INL) + OPL, Photoreceptor Inner Segments (PIS), and Photoreceptor Outer Segments (POS).

Bagci *et al.* (44) were able to detect six different retinal layers, which are NFL, IPL + GCL, INL, OPL, ONL + PIS, and POS from normal healthy eyes. Lu *et al.* (45) identified and measured the thickness of six layers extracted from 3D images of healthy subjects. These layers were NFL, PIS, POS, Retinal Ganglion Cell (RGC), IPL, and OPL. Rossant *et al.* (46) detected eight layers from healthy subjects. Yang *et al.* (47) detected nine boundaries from 3D images of healthy and glaucomatous eyes.

Shi *et al.* (38) were able to segment ten retinal layers in 3D images of patients with retinal pigment epithelial detachments (PED). Sugrk *et al.* (39) proposed a segmentation method to find the retinal pigment epithelium (RPE) layer and to detect a shape of drusen in this layer. Then, the RPE layer is used to find retinal nerve fiber layer (RFL) and to detect a bubble of blood area in RFL complex. ElTanboly *et al.* (48) detected 12 different layers, which are NFL, GCL, IPL, INL, OPL, ONL, External limiting membrane (ELM), Myoid Zone (MZ), Ellipsoid Zone (EZ), Outer Photoreceptor (ORP), Interdigitating Zone (IZ), and RPE layers. Figure 2 shows an OCT retinal image with its 12 distinctive layers for a typical healthy person.

The focus of this survey is to discuss the current findings in OCT retina images with respect to the effect of different diseases on the retina layers. We will discuss the current studies for each disease and how it affects the structure of the various layers in OCT images. We will concentrate on the methodologies of handling different OCT images for normal and diseased retinas. Then, we will discuss the current challenges and research topics in this field.

3. RELATED WORK

As previously mentioned, OCT images can be used to show the structure of the retina. The detected layers in the OCT retinal images can be utilized as an indicator for healthy and diseased eyes. Recently, there are many studies, which are conducted to analyze the OCT retinal images to classify the healthy from diseased patients. Each disease can be classified depending on some characteristics that can be absent or found in the OCT images. In the next subsections, we will discuss the current work in normal eyes as well as the diseased eyes. We will begin with the detection of the retina's layers in healthy persons. Then, we will discuss the characteristics and studies of the most common diseases, which can be indicated by the analysis of the OCT retinal images.

3.1. Normal healthy eye

As OCT has histological correspondence, the interpretation of the OCT image seems to be quite intuitive. However, OCT technology depicts tissue reflectivity. It is dependent on the tissue optical properties, i.e. microscopic variations in the refractive index of subcellular structures, and on the amount of light signal that the tissues absorb (49, 50). When analyzing an OCT image for retina, there

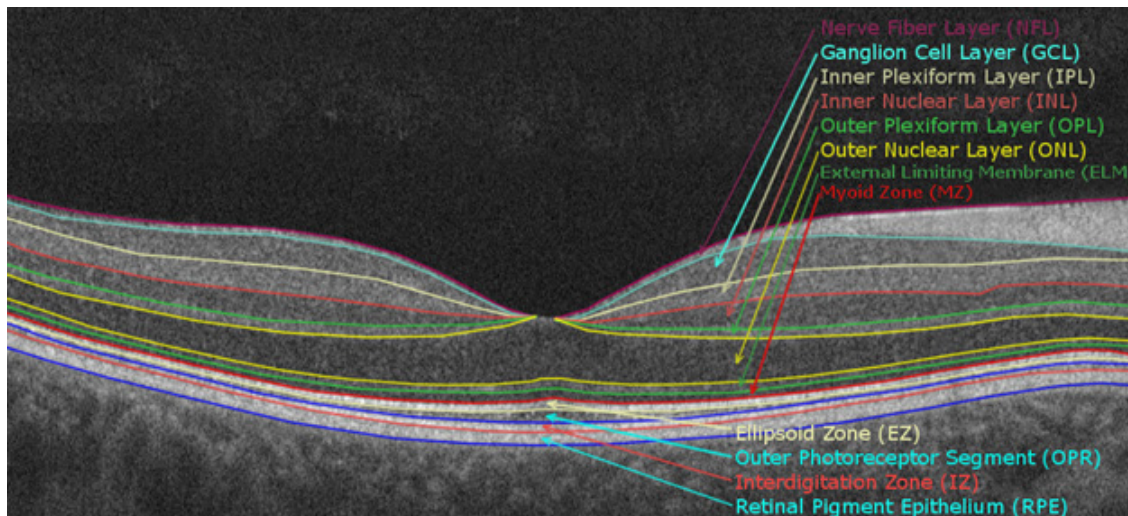


Figure 2. OCT retinal image with its distinctive 12 layers for a typical healthy person in macular region of retina.

is no standard for the number of layers. Most studies estimate four, seven, ten, eleven, or twelve layers. On the other hand, normal retinal thickness differs from one device to another due to different characteristics, such as age, gender, race, and refraction. In addition, all measurements using SD-OCT have higher values than using TD-OCT due to the higher resolution (51).

Bagci *et al.* (44) detected six different layers (NFL, IPL+GCL, INL, OPL, ONL+PIS, and POS) in OCT retinal images. They proposed an algorithm that was able to segment retinal layers. This algorithm is developed based on 2D edge detection scheme that suppresses speckle noise and at the same time enhances the edges along the retinal depth. A gray level mapping technique was proposed to overcome uneven tissue reflectivity and variance across subjects. Their system was tested only on normal subjects. The tested images were taken by two different OCT devices. First, images of 15 normal subjects were taken using the Stratus OCT device with the average of their ages was (57 ± 11) years old. Second, images of 11 normal subjects were taken using RTVue OCT device with average age equals to (56 ± 7) years old. The thickness of all the layers was measured and compared with the results of 3 manual observers. The mean absolute values were between 3–4 μm between the automated and manual thickness measurements. Additional work is needed to prove the ability of this proposed system to deal with images that are obtained from patients with different retinal diseases.

Rossant *et al.* (46) determined eight layers (RNFL, ONL, GCL+IPL, INL, OPL, IS, OS, RPE) in high-resolution OCT images. They proposed a segmentation method for detecting the layers by using the knowledge about the relative position of the layers. The system used 25 normal subjects with 72 images. Fourteen images were chosen to be manually

segmented by five experts. They calculated the distance between the manually traced curves and the ones obtained by the proposed method. The measures that are manually performed by the experts and those obtained from the automatic segmentation were very close. This algorithm was tested only on normal eyes. In addition, it lacked more details about the evaluation of the proposed technique. They noticed a change in the profile of the fovea with the axial length. When the central ONL thickness increased, the foveal thickness increased. A significant variability of the OPL/ONL complex was noted independently of axial length. The maximal retinal thickness was stable over a large range of axial length and had a low coefficient of variation. Finally, no differences that are related to gender were noted.

Lu *et al.* (45) detected and measured the thickness of six different layers (RNFL, IS, OS, RGC, IPL, and OPL) in OCT retinal images. The proposed segmentation algorithm cut the OCT image into the vessel and non-vessel sections. First, the vessel section is detected by the polynomial smoothing procedure. Then, the non-vessel section was filtered using two filters, which were bilateral and median filters. The layers were then detected and classified. For the layers in the vessel section, they were defined using linear interpolation of the layer boundaries that were detected in the non-vessel section. The system was tested using the images of four healthy subjects. There was more error in the thickness measure at the vessel section. Errors varied due to different image noise level and layer boundary quality. Errors were occurred more often in measuring the thickness of RNFL. The algorithm measured it thicker than it should be. This algorithm needs advanced image interpolation techniques to improve the layer boundaries of the vessel sections. In addition, it requires other advanced image smoothing techniques, which are important to

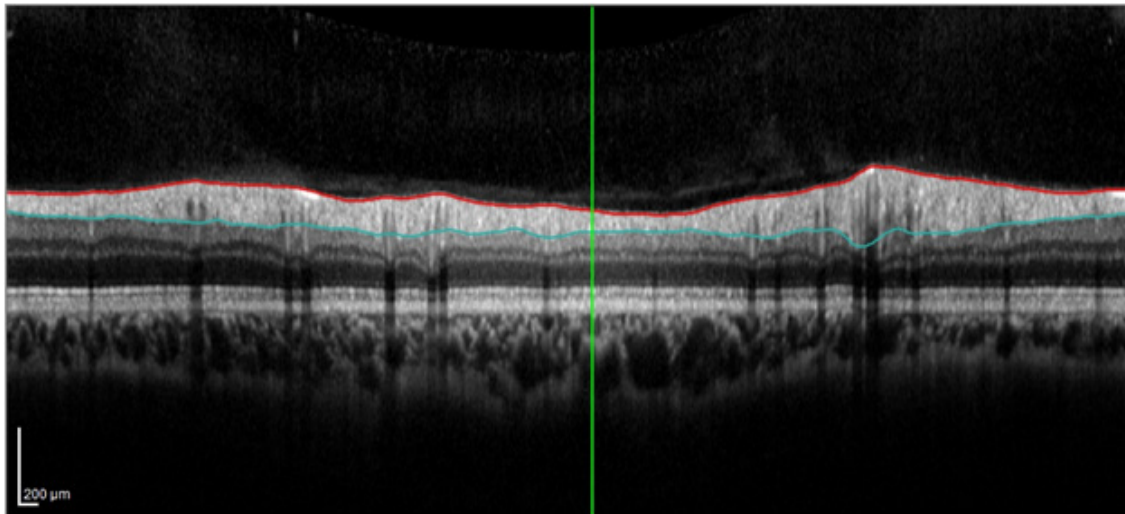


Figure 3. OCT retinal image for a glaucoma patient.

be able to segment non-RNFL layers that are often much thinner than the RNFL. The algorithm needs to be evaluated over a larger dataset.

Kajić *et al.* (4) detected and built the thickness maps for eight intraretinal layers in normal eyes. First, they learned the variation parameters from the training data that were manually segmented. Then, these parameters were used to drive a model to able to segment unseen data. The algorithm was evaluated against a large set of images that were manually segmented. 466 images from 17 eyes were manually segmented twice by two different persons using Amazon Mechanical Truck workers (AMT). This algorithm could produce accurate results even in the existence of strong speckle noise. It showed only a larger variation around the foveal region. Even when they added background noise to the images, the algorithm showed robust performance. On the other hand, further investigation is needed to test the proposed algorithm on patient subjects.

Salarian *et al.* (52) proposed a method to detect certain layers using graph theory and the shortest path algorithm. They chose the Regions of Interest (ROI) that could be used in normal cases and some abnormal ones. They discovered that by changing some parts, such as ILM, RNFL, and RPE, these layers could be found easily. They applied the proposed technique to all B-Scan images of 16 people, including low-quality images and some images with diseased eyes. The results were accurate based on manual segmentation of an expert. In the future, they can apply other ways of weighting or use other types of information to improve the proposed method. This modification can be useful for savior diseased cases.

Lang *et al.* (40) adapted the N3 framework that was originally implemented to correct MRI data for

intensity inhomogeneity correction in OCT images. To create a template intensity profile for each layer, they transformed the data to a flattened macular space, which afforded an accurate initial estimate of the gain field. To correct the data, N3 produced a smoothly varying field. Their proposed methodology was capable of both recovering synthetically generated gain fields and improving the stability of the layer intensities. They made manual segmentation for 41 OCT images. They delineated nine boundaries on every B-scans.

3.2. Glaucoma

Glaucoma is a set of neurodegenerative eye diseases that leads to the loss of vision and blindness. It is the second leading cause of blindness in the world (53). Both NFL thickness and the Euclidian distance between NFL and the Inner Limiting Membrane (ILM) can be used as markers for the glaucoma disease. The glaucoma patient has a decreased NFL thickness as compared to the typical healthy subjects. Recently, it has been said that both of the choroid thickness and a measure of separation between Bruch's Membrane (BM) and choroid can also be used as a marker of the glaucoma disease (54). Figure 3 shows an OCT image for a glaucoma patient.

Many studies have been made to diagnose the glaucoma disease depending on OCT retinal images. For example, Ishikawa *et al.* (55) detected four various layers (macular nerve fiber layer (mNFL), inner retinal complex (IRC), OPL, and outer retinal complex (ORC)) in OCT retinal images. They applied an adaptive thresholding technique to search for borders of retinal layer structures on each sampling line. They tested their system on normal and glaucomatous subjects. They used 16 subjects for training (5 normal and 11 affected by glaucoma disease) to assess their proposed system. The average ages for normal and

diseased subjects were (52.1 ± 14.8) and (62.4 ± 14.5) years old, respectively. On the other hand, they used 64 subjects for testing their proposed system (27 normal and 37 glaucomatous). The algorithm failed to detect the layers with 55.6% in poor quality images and failed with 10.2% in good quality ones. The ILM layer was the most reliable board, while the IRC layer was the least reliable one. From the experimental results, they found that in normal subjects the mFNL, IRC, total retinal thickness, and cpNFL were thicker. The best-performing macular segmentation parameter in this study was mNFLIRC thickness. To improve the overall performance of this system, they need to use better methods and procedures for preprocessing, filtering, and border detection.

Yang *et al.* (47) detected the boundaries between some retinal layers by proposing an automated boundary segmentation algorithm for 3D OCT images. First, a customized Canny edge detection was used to create a map that showed main local edges. Then, a graph was built based on the axial intensity and the Canny edge map. Finally, the layers were extracted using the shortest path search through the graph. The algorithm was able to define nine different boundaries. These boundaries were the ILM boundary, the boundary between NFL and GCL, the one between GCL and IPL, the one between IPL and INL, the one between INL and OPL, the ELM boundary, the one between IS and OS, the one between OS and RPE, and the one between BM and Choroid. The algorithm was tested on 19 healthy subjects and 19 with glaucoma disease. The results were compared with the results from four manual segmentation experts. The difference between the measurement of ILM, INL/OPL, and BM/Choroid boundaries versus the manual segmentation was very close to the difference between segmenters. The NFL/GCL and IPL/INL versus the manual segmenters were larger than between segmenters but when the Fovea area was excluded the difference was improved. The problem in the NFL/GCL boundary was on the side where NFL is thin. It was detectable, but it was detected thicker. This algorithm, even in the poor quality image (low intensity, and low contrast) still able to detect the boundary. The algorithm notices that the NFL was clearly thinner in the glaucoma patients.

Varmeer *et al.* (56) worked on 3D images to detect six retinal layers (vitreous, RNFL, GCL + IPL, INL + OPL, Photoreceptor + RPE, and Choroid). The proposed system worked well for both normal and diseased eyes with glaucoma. It was able to build the thickness maps for single or combined layers. The algorithm used ten healthy subjects and eight subjects with glaucoma. Two scans held manually for the healthy ones, and one scan for the diseased one. RMS errors were between 4 and 6 μm for the top and bottom of the retina. The errors for intra-retinal interfaces were between 6 and 15 μm . The resulting

total retinal thickness maps corresponded with known retinal morphology. They compared RNFL thickness maps with GDx (Carl Zeiss Meditec) thickness maps, and both were mostly consistent. In OCT-derived thickness maps, local defects, which are found in temporo-superior and temporo-inferior regions, were better visualized. In the two cases of glaucoma, the RNFL is thinner than in the normal eye.

Kafieh *et al.* (5) introduced a segmentation technique based on a variant of spectral graph theory, which was called diffusion maps. It relied on regional image texture in localizing boundaries *in situations* of low image contrast and poor layer-to-layer image gradients. Their proposed method was based on the application of two sequential diffusion maps. The first one segmented the ILM-to-RPE. The second one localized the internal layers between the ILM and the RPE complexes. To partition the data into important and less important sections and to localize the internal layer. They applied this method to 2D and 3D OCT data sets. In experimental results, they tested the proposed technique on 23 images data set from two groups (normal and glaucoma patients). The mean unsigned border positioning errors (mean \pm SD) was $8.52 \pm 3.13 \mu\text{m}$ for a 2D method and was $7.56 \pm 2.95 \mu\text{m}$ for the 3D method.

Bogunović *et al.* (57) proposed an algorithm to segment intraretinal layers of OCT images. After 2D “en-face” alignment, all the fields were segmented simultaneously. To penalize deviations from the expected surface height differences for each pair of overlapping fields, they imposed a priori soft interfield-entrasurface constraints. They were extracted to be the depth-axis shifts, which produced the maximum cross-correlation of pairwise-overlapped areas. The algorithm could segment 11 surfaces, but the evaluation was focused on only four surfaces to the ease of manual tracing. These surfaces are ILM, the surface between NFL and GCL, the surface between IPL and INL, and the outer boundary of RPE. These four surfaces enabled the algorithm to compute the thickness of NFL, GCL + IPL, and total retinal thickness. The method was evaluated using 180 images acquired from 10 glaucoma patients (three severe, five moderates, two mild). The obtained average error was $(4.58 \pm 1.46) \mu\text{m}$, which was comparable to the average difference between different observers $(5.86 \pm 1.72) \mu\text{m}$. The overall mean thickness per patient was $(1.07 \pm 0.35) \mu\text{m}$ for NFL, $(0.73 \pm 0.31) \mu\text{m}$ for GCL+IPL, and $(1.86 \pm 0.35) \mu\text{m}$ for total retinal.

3.3. Central serous chorioretinopathy (CSC)

CSC is a chorioretinal illness, which is not understood completely with systemic associations. It has a multifactorial etiology with a very complicated pathogenesis. Ophthalmoscopic indications of CSC

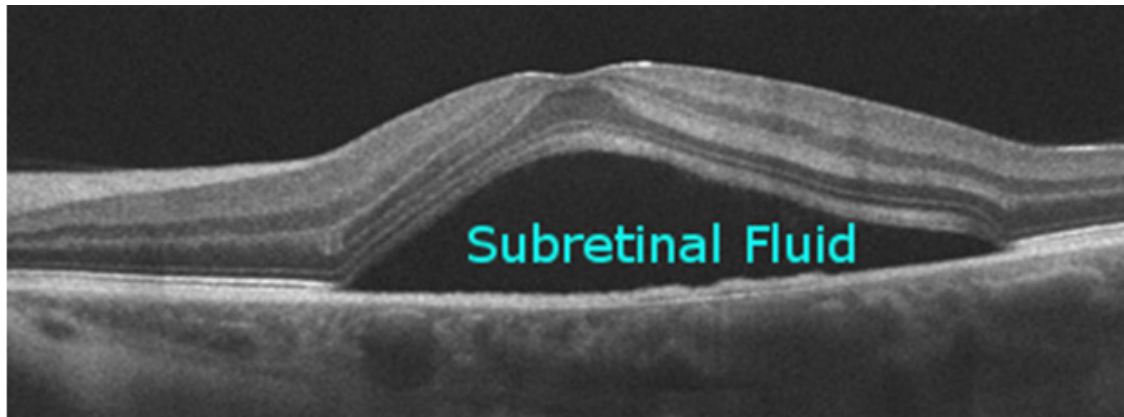


Figure 4. OCT retinal image for a CSC patient.

range from mono- or paucifocal RPE lesions with a noticeable increase of the neurosensory retina by clear fluid (regular in recent onset cases) to shallow detachments overlying large patches of irregularly depigmented RPE (58). Because of the fluid that is accumulated under the retina distortions or visual loss may appear. In normal and CSC diseased subjects, the 3D configuration of the subretinal fluid differs (59). So, detecting these changes in both of fluid and RPE can help in diagnosing this disease. Figure 4 shows an OCT retinal image for a CSC patient.

Some studies were done to diagnose the CSC patients by analyzing the OCT retinal images. For example, Eandi *et al.* (60) determined the foveal thickness and anatomical changes in the fovea and visual acuity in unilateral resolved CSC patients. In this study, 20 patients were involved with an age range between 31 to 66 years old. They normalized the foveal thickness by dividing its value by the uninvolved fellow eye value. The best-corrected visual acuity was normalized also. Patients with unilateral resolved CSC had a decreased central foveal thickness. Therefore, there was a correlation between this thickness and the visual acuity. In addition, there was the inability to observe the ELM layer in most of the diseased eyes. There was also difficulty in observing the boundary between the photoreceptor bodies and the outer segments. All these observations were correlated with visual acuity.

Imamura *et al.* (61) evaluated the choroidal thickness in patients with CSC disease. The thickness of the sub-foveal choroidal was measured from the inner scleral border to the outer border of the retinal pigment epithelium. In this study, 19 patients with 28 eyes were involved. The mean age of them was 59.3. The measured choroidal thickness was $(505 \pm 124) \mu\text{m}$, which was much greater than the choroidal thickness in normal eyes ($P \leq 0.001$).

Novosel *et al.* (41) presented a locally adaptive approach based on loosely-coupled level sets to segment the fluid and the interfaces between retinal layers in eyes affected by CSR. The approach exploited the local attenuation coefficient differences of layers around an interface. To delineate the fluid, the approach introduced auxiliary interfaces. The approach could handle abrupt attenuation coefficient variations and topology disrupting anomalies. The mean absolute deviation for the interfaces was $3.7\text{--}8.9 \mu\text{m}$ (1–2 pixels), and the Dice coefficient for the fluid segmentation was 0.96 compared to a manual segmentation. They segmented the retinal layers and fluids simultaneously. So, they aided each other in retrieving the right segmentation. An error of $3.9 \mu\text{m}$ corresponded to one pixel along the A-lines. The accuracy showed an RMSE ranging from $4.4 \mu\text{m}$ to $13.4 \mu\text{m}$ and a MAD ranging from $3.7 \mu\text{m}$ to $8.9 \mu\text{m}$. The Dice coefficient, TPR, and FPR were 0.96, 95%, and 1%, respectively.

3.4. Unilateral anterior ischemic optical neuropathy (AION)

AION is causing damage to the optic nerve from inadequate blood supply that results in loss of vision. There are two main types of AION: Arteritic AION (AAION) and Non-arteritic AION (NAION or AION). In NAION, the retinal NFL layer thickness is significantly increased in the acute stage. Then, it is significantly decreased in the resolving stage. In the sequent paragraphs, some of the current work concerning both types of the AION diseases is discussed.

Garvin *et al.* (43) detected five layers (NFL, GCL+IPL, INL+OPL, IS, OS) in OCT retinal images. The layers were identified by finding a minimum-cost closed set in a constructed geometric graph. This graph is constructed from the edge/regional information and a priori determined surface smoothness and interaction constraints. This study was conducted on

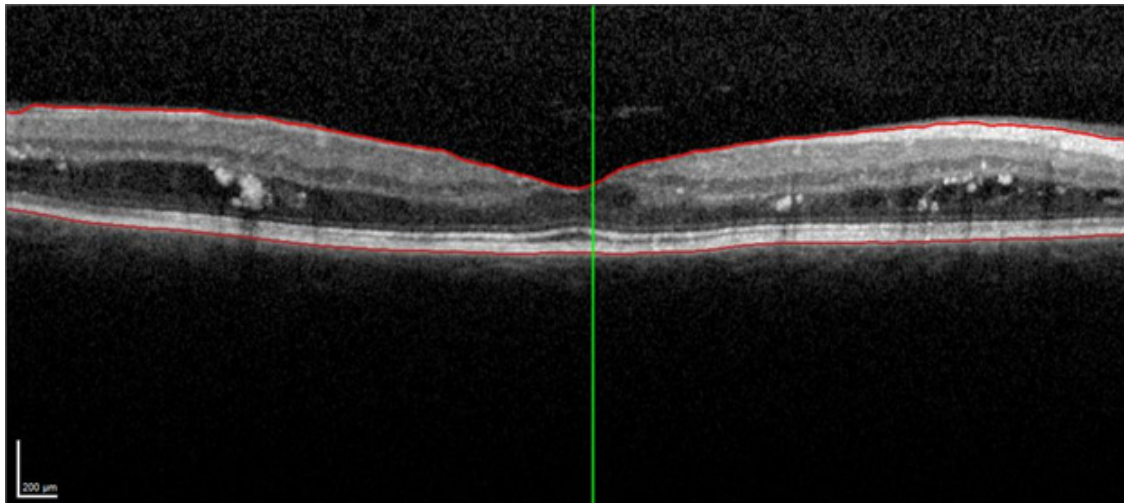


Figure 5. OCT retinal images for a DME patient.

3D images for 12 patients with AION disease for one eye or both. They observed that there were changes in both the inner and the outer retinal thickness for the affected eye. The inner retinal thickness was $24.1 \mu\text{m}$ smaller than unaffected one, and the outer retinal thickness was $3.7 \mu\text{m}$ smaller in the affected eye. The results were compared with the results of 3 manual observers. The border positioning errors and thickness differences between the observers were very close to those of the results and the reference standard. Their algorithm attempted to segment all surfaces although sometimes some layers are not present. In some images, surface two might not be visible, and some images were too noisy to resolve the layer boundaries.

Garvin *et al.* (62) provided two extensions of their previous work. The first extension was the ability to incorporate varying feasibility constraints and capacity to incorporate true regional information. The second was that they applied a new method on retinal layers in SD-OCT images. Therefore, their proposed method extracted seven surfaces from the processed images. In addition, they found that the bigger coverage of the macular region generated a greater variation of layer appearances.

Hedges *et al.* (63) demonstrated the existence of subfoveal fluid, which was associated with optic disc swelling from NAION. In this study, 76 patients were involved. Eight patients had apparent subretinal fluid that extended into the subfoveal space. The visual acuity was improved in five of these eight patients as the subfoveal fluid resolved. However, they concluded that the subretinal fluid was developed in some patients with NAION. In addition, they found that this disease might cause visual acuity loss.

3.5. Diabetic macular edema (DME)

DME can cause vision loss in persons with diabetes mellitus. It can be defined as a blood leakage pass in RPE layer and photoreceptor inner/outer segment (IS/OS) from choroid into the RNFL complex. The visual ability is lost by increasing the area of the blood or bubble that is found in the RNFL complex. In the United States, there are approximately 26 million persons suffering from DME (39, 64). OCT modality is used to find the presence of the blood area or bubble in the RNFL complex. In addition, the diagnosis of the DME can be made by measuring the variation of the thickness in some retinal layers. Figure 5 shows an OCT retinal images for a DME patient.

Due to fluid accumulation that can be intra- or extra-cellular, DME increases the retinal thickness. Due to the increased fluid intake, the cells are enlarged in intra-cellular edema. Otherwise, extra-cellular edema results from fluid accumulation outside the cell. In the second type of edema, hard exudates can be structured because of the lipid contents of the leakage can agglomerate into an irregular shape. Finally, each eye of a DME patient can present regions with different characteristics, such as increased ONL thickness, cysts, and even areas without any visible changes (65).

Current studies have shown that the visual acuity can be predicted by the volume of retinal tissue within fluid-filled spaces (66). Further, clinical studies based on the volume of cystoid fluid and the location of the cysts may be used as a metric for visual prognosis. Additionally, the presence of diabetic cysts may alter the normal pattern of the sub-retinal layers leading to sub-retinal disorganization. The extent of

disorganization can be estimated using a method of localizing these cysts in certain sub-retinal layers (67).

Roychowdhury *et al.* (67) localized cysts in OCT images for patients with DME. In each image, Six sub-retinal layers were identified using an iterative high-pass filtering approach. Then, dark regions were detected as candidate cystoid regions. To estimate the area of cystoid regions, each candidate cystoid region was analyzed using solidity, mean, and the maximum pixel value of the negative OCT image as decisive features. This algorithm was capable of determining the boundaries of contiguous cysts by breaking down large cysts. This system was able to detect cystoid area with 4.6% mean and 6.6% standard deviation based on 120 OCT images of 25 DME patients. This method achieved 100% sensitivity and 75% specificity in separating images with no cysts from the ones with cysts. In addition, it achieved 90% correlation between the manually segmented area and the cystoid area defined by the algorithm. This algorithm located the cysts in the inner plexiform with an accuracy of 88%, in inner nuclear with an accuracy of 86%, and in outer nuclear regions with an accuracy of 80%.

Roychowdhury *et al.* (53) produced 3D thickness maps for images of normal subjects and patients with DME. The first stage of the proposed algorithm was to make de-noising for OCT images. Then, they applied the automated segmentation method to extract the layers using multi-resolution high pass filtering. They extracted only six retinal layers (NFL + IPL, INL, ONL, Inner layer, and Outer Layer) with their thickness from all the tested images to form the thickness maps. They applied this system to 203 normal images from 10 healthy subjects and 357 images from 15 patients with DME. They measured the correlation coefficient (r) between the results of the proposed system and the manual segmentation. They obtained $r > 0.8$ in normal cases and $r > 0.7$ in abnormal ones. They found that the thickness of the inner layer with DMA was 1.12 times more than normal cases. In DME cases, the INL layer appeared relatively thicker, and the ONL layer appears irregular and exceeding 200 μm . Therefore, the thickness maps of the INL and ONL could be used as an indicator of disease severity and for tracking the changes in DME patients over time.

Correia *et al.* (65) identified the changes happened to ONL layer in DME patients. The OCT images were obtained from healthy subjects as controls and patients with DME. The images were distributed into three groups. These groups were healthy subjects, DME patients where ONL thickness was significantly increased, and DME patients with normal thickness for ONL. For all processed images, the ONL was segmented and processed to produce a representative A-scan. They used the optical and

physical characteristics of the healthy human retina as a reference in their proposed system. They used a Monte Carlo technique with a model for the ONL to simulate an A-scan for each group and compare it to the real OCT data. The results showed that there were two types of edema, cytotoxic (intra-cellular) and vasogenic (extra-cellular). In the DME without changes in the ONL group, the most observed feature for the real OCT data was the increase in the volume of the nucleus. The data of patients with DME with increased ONL could be created by increasing ONL thickness from the healthy status by the exact increase in ONL thickness.

Abhishek *et al.* (68) segmented the intra-retinal layers for edema patients and normal subjects. The segmented layers were ILM and RPE layers. The graph-based segmentation was solely based on pixel intensity variation and distance between neighbor pixels. They used the weighting scheme and shortest path search to identify the neighborhood pixel. In this algorithm, the preprocessing step could be considered as optional. There were 12 diseased images and 9 normal images. The algorithm was able to detect ILM and RPE layers in 7 out of 9 normal subjects and 11 out of 12 DME affected subjects due to expert validation. It was found that the range of the thickness of the normal subject was less than 50, whereas the range of the DME subjects was more than 50. In some cases, it even reached 200. So, the thickness could be used as a good sign of the presence of edema. In this method, if they limit the search regions it can detect the other retinal layers. Another advantage of this method is that it is less prone to noise.

3.6. Cystoids macular edema (CME)

CME occurs in a variety of diseases like diabetic retinopathy, AMD, retinal vein occlusion, and intraocular inflammation (69). It affects the full-thickness of the retinal tissue involving the anatomic fovea (70). It appears more often in people over 60 years old. It affects visual acuity and may lead to loss of vision or even blindness. Figure 6 shows an OCT retinal image for a CME patient.

There are some current studies that discuss the diagnosis of CME disease from analyzing the OCT retinal images. For example, Zhang *et al.* (71) determined the volume of CME for the retinas with macular hole (MH) in 3D OCT images. Their system consisted of three main phases, which were preprocessing, coarse segmentation, and fine segmentation. The preprocessing phase included de-noising, intraretinal layers segmentation and flattening, and MH and vessel silhouettes elimination. An AdaBoost classifier was used to get the seeds and constrained regions for graph cut in the second phase. In the last phase, a graph cut algorithm is used to

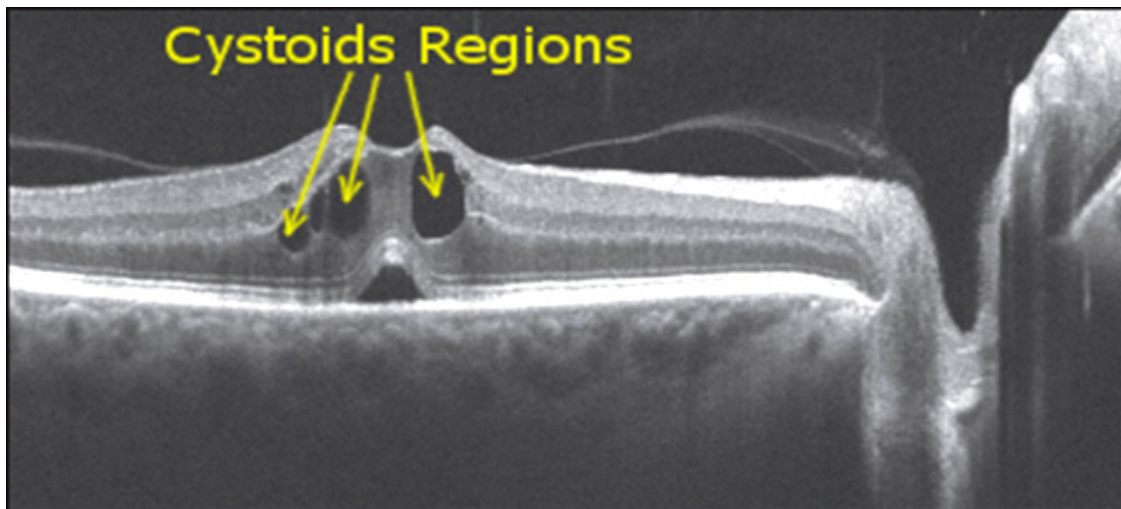


Figure 6. OCT retinal image for a CME patient.

get fine segmentation results. The proposed system was evaluated by 3D OCT images from 18 patients with CMEs and MH. The true positive volume fraction (TPVF) was 84.6%, and the false positive volume fraction (FPVF) was 1.7%. The accuracy rate (ACC) for CME volume segmentation was 99.7%. For the validation, a leave-one-out strategy was used during training and testing. Supervised by an experienced ophthalmologist, the CME regions were segmented manually to work as ground truth. However, a more accurate shape model of the MH (includes the maximum/minimum diameter of the MH) was needed. In addition, the proposed system detected the obvious cyst only.

Slokom *et al.* (72) identified CME regions in SD-OCT of the macula. An algorithm was made to detect cystoids. First, it identified the borders of the cystoids. Then, to obtain surface area of fluid in the image, a quantitative analysis of liquid in cystoids regions was made. They used data from six patients with CME associated with diverse retinopathy. In the central part of the retina, two patients had a singular cystoids region, and the others had multiple cystoids regions. They applied the distribution metric for image segmentation that appeared as a result from prediction theory to detect cystoids in OCT images. Applying level set process, an energy model based on the metric was incorporated into the Geometric Active Contour (GAC) algorithm. The clinical expert classified the extracted results from every image as good and fair extraction. 95% were classified as good and fair extraction cases. The average precision was 95.02%, and average sensitivity was 88.46%. The area of each cystoids region was calculated and compared to the manual extraction, which was in all cases smaller than those of the clinical expert.

3.7. Age-related macular degeneration (AMD)

AMD is a degeneration of the eye that is leading to severe visual impairment and visual loss for people who are 55 years old or older. In the United States, there are approximately 8 million persons who have monocular and binocular AMDs. This disease is detected by searching for drusen, which is defined as abnormality between the basal lamina of RPE and the inner collagenous layer of BM (73, 74). Figure 7 shows an OCT retinal image for AMD patient.

Khanifar *et al.* (75) categorized the drusen ultrastructure in AMD using OCT retinal images. A sample of 31 eyes of 31 AMD patients was utilized in this study. The images were analyzed, and the drusen were scored by four categories, which are shape, predominant internal reflectivity, homogeneity, and the presence of overlying hyper-reflective foci. They calculated the spread of each morphologic pattern and the combinations of the extracted morphologic patterns. 21 images were chosen for the adequate quality. 17 drusen were found from 120 drusen in the whole images. Most of the found drusen were convex, homogeneous, with medium internal reflectivity, and without overlying hyper-reflective foci. Non-homogenous drusen were found in 16 eyes, five of them have a distinct hyper-reflective core. Hyper-reflective foci overlying drusen were in 7 eyes.

Schuman *et al.* (76) detected the changes in the retina using OCT images in AMD patients. 17 eyes of 12 patients with nonneovascular AMD and drusen were used. 17 eyes of 10 age-matched were used as a control. Over 97% of drusen, the PRL was thinned. The average PRL thickness was reduced by 27.5% over drusen. They found that difference was valid and significant ($P=0.004$). They observed two

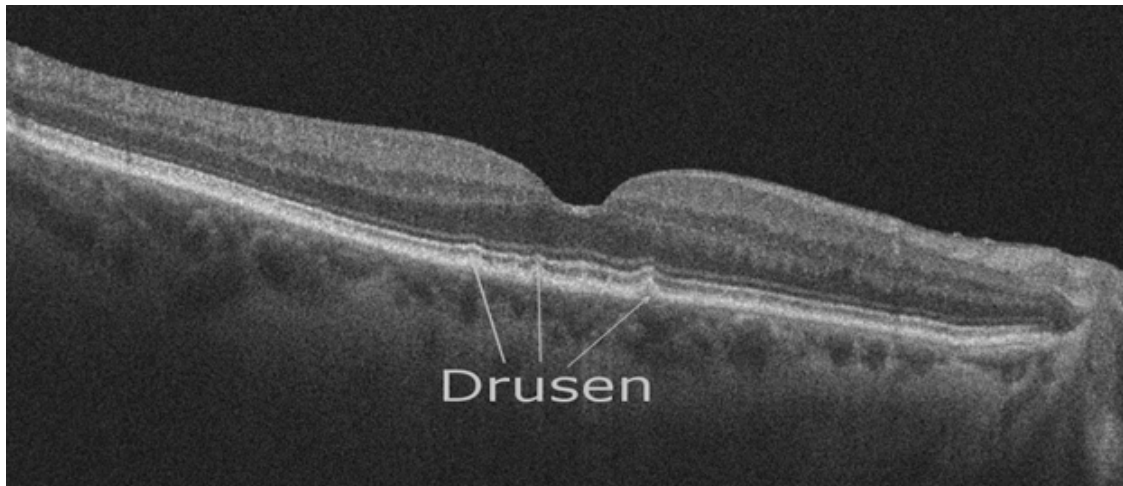


Figure 7. OCT retinal image for an AMD patient.

types of hyperreflective abnormalities over drusen in the neurosensory retina. Finally, they concluded that distinct hyperreflective speckled patterns occur over drusen in 41% of AMD eyes and never in control eyes.

Oliveira *et al.* (77) proposed a method to integrate sparse higher order potentials (SHOPs) into a multi-surface segmentation framework. It was used to confront with local boundary variations caused by drusen, which was important to evaluate AMD progress. The mean unsigned error for the inner retinal pigment epithelium (IRPE) was $5.65 \pm 6.26 \mu\text{m}$ and for BM was $4.37 \pm 5.25 \mu\text{m}$. The results were comparable to those obtained by two experts. Their average inter-observer variability was $7.30 \pm 6.87 \mu\text{m}$ for IRPE and $5.03 \pm 4.37 \mu\text{m}$ for BM. The IRPE and the other boundaries were successfully segmented. Their proposed technique was evaluated in a data set of 20 AMD patients. The data set also included manual segmentations of the ILM, IRPE, and BM boundaries performed by two expert graders.

3.8. Other different diseases

In this section, we discuss other work that does not lay under any of the above diseases or research studies that deal with more than one disease. First, we discuss the PED, which is considered as a notable feature of many chorioretinal disease processes, including AMD, polypoidal choroidal vasculopathy, central serous chorioretinopathy, and uveitis. It can be classified as serous, fibrovascular, or drusenoid.

Shi *et al.* (38) proposed a framework for segmenting the retinal layers in 3D OCT images with serous retinal PED. Their framework consisted of three main stages. The first stage was the fast de-noising and B-scan alignment. The second stage was the multi-resolution graph search based surface detection. Finally, the third stage was the PED region detection

and surface correction above the PED region. They evaluated their system by using 20 PED patient. The experimental results showed that the TPVF was 87.1%, the FPVF was 0.37%, the positive predictive value (PPV) for PED was 81.2%, and the average running time was 220s for OCT data of $512 \times 64 \times 480$ voxels.

On the other hand, Sugruk *et al.* (39) proposed a segmentation technique to divide OCT images to detect the shape of the drusen in the RPE layer. They used the RPE layer to find RFL layer to detect a bubble in the blood area. They used binary classification technique to classify AMD and DME diseases depending on the retrieved characteristics. They used only 16 OCT images (10 images for AMD and six images for DME) in their experiments. Their proposed classification system achieved 87.5% for accuracy.

ElTanboly *et al.* (48) proposed a segmentation framework for retinal layers from 2D OCT data. Their framework was based on the joint model, which included shape, intensity, and spatial information. It could segment 12 distinct retinal layers in normal and diseased subjects. The shape was built using a subset of co-aligned training OCT images, which were initially aligned using an innovative method to employ multi-resolution edge tracking. Then, the visual appearance features were described using pixel-wise image intensities and spatial interaction features. A linear combination of discrete Gaussians was used to model the empirical gray level distribution of OCT data. To eliminate the noise, they integrated the proposed model with a second-order Markov-Gibbs random field (MGRF) spatial interaction model. They tested their framework on 250 normal and diseased OCT images with AMD, and DR. Their proposed segmentation method was evaluated using Dice coefficient ($\text{DSC} = 0.763 \pm 0.1598$), agreement coefficient ($\text{AC1} = 73.2 \pm 4.46\%$), and

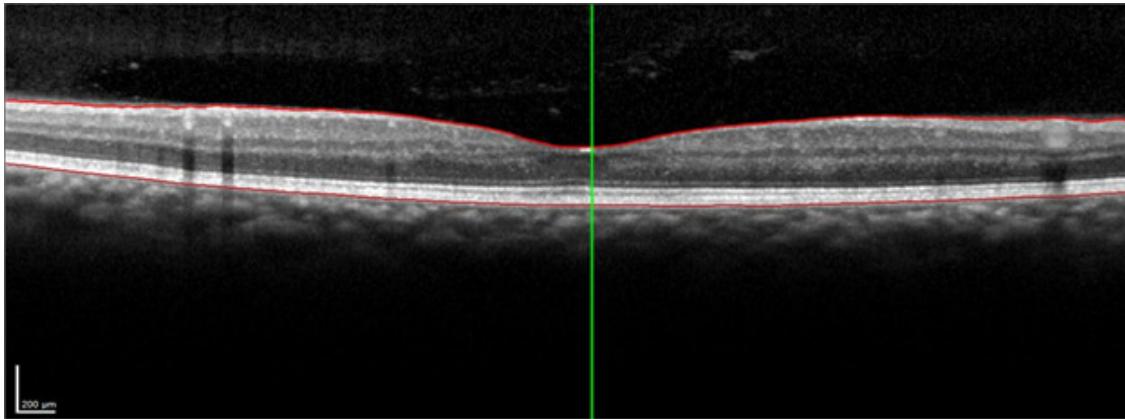


Figure 8. OCT retinal image for a DR patient.

average deviation distance ($AD=6.87\pm2.78\ \mu\text{m}$) metrics. Figure 8 shows an OCT retinal image for a patient with Diabetic Retinopathy (DR).

4. CHALLENGES AND FUTURE DIRECTIONS

As previously mentioned, the OCT image modality provides a great diagnosing aid for many organs. It is used in a wide range for diagnosing retinal diseases, such as glaucoma, CSC, AION, DME, and CME. Many studies were conducted to extract some specific features from OCT retinal images to diagnosis some diseases. In this section, we will discuss some challenges, which are currently facing the analysis of OCT retinal images. In addition, some future research directions will be discussed briefly in the sequent points.

4.1. Automatic segmentation techniques

OCT devices nowadays produce a large number of images. This large number of images make it difficult for humans to investigate. In addition, the existence of speckle noise, low image contrast, irregular shapes, morphological features (retinal detachment, macular holes, drusen), accurate manual segmentation of retinal layers is considered as a difficult task (43). So, there is a need to produce automatic segmentation techniques to handle this large number of images. Automatic segmentation techniques can reduce time and effort. Also, they can provide repeatable and quantitative results (78). They should be accurate and robust to image degeneration and low signal to noise ratio. It can allow early diagnosis or therapy monitoring. Thickness measurements are necessary for detecting pathological changes and diagnosing of retinal diseases (44). Nevertheless, a few segmentation approaches have been developed, which addressed the problem of layers that are either invisible or missing (79, 80). The proposed technique should be robust with respect to different types of OCT scanners from different manufacturers. They also

should be robust with respect to the presence of blood vessel artifacts in the OCT images (5).

4.2. OCT CAD systems

Regarding the current work in OCT CAD systems, the experimental results show that these systems are used in offline clinical or pathology studies. Therefore, additional speed-up is required for OCT CAD systems to become suitable for clinical practice (38).

4.3. Standard number of layers

As far as we know, there is no standard number of detected layers in OCT retinal images. Some studies prefer to define all intraretinal layer, whereas other studies prefer only to define the most critical retina layers that are needed to identify a disease.

4.4. Weak layer boundaries

The target layers in the retina lack strong boundaries, which are surrounded by tissues with similar intensity profile. In addition, many objects are laying in a small region (45, 81).

4.5. Artifacts

There are many types of artifacts that are found in OCT images. Intensity inhomogeneity is considered as an important reason that significantly affects the accuracy of the segmentation process of the retina layers (82). There are many reasons for intensity inhomogeneity in OCT images, such as poor scan quality, after multi-frame averaging, opacity of transparent ocular media, off center acquisitions, and vignetting due to misalignment. This problem negatively affects the performance of the used processing techniques, especially the segmentation process. Finally, little work had been done to correct this issue (40).

5. CONCLUSION

OCT images have made it more easy to identify the structure of normal and diseased retina, which can be used for early diagnosis of several diseases and monitor the effect of the treatment. OCT is one of the fast developing medical image modality in the last decade. It uses low coherence interferometry to map out back-scattering properties from different depths of samples. Various retinal diseases can be detected efficiently by analyzing the OCT retinal images. Each retinal disease has some specific features, which can be effectively detected in OCT images. In this paper, we reviewed how OCT is capable of defining the structure of normal eye retinal layers as well as the structure of the diseased ones. We presented an overview of the current processing techniques as well as how can they be applied to help in the diagnosis and treatment of the diseased eyes. In addition, we defined some of the challenges that face scientists in analyzing and extracting the necessary information from OCT retinal images. The promising experimental results for the reviewed techniques in a variety of clinical applications suggest that OCT is a clinically relevant imaging modality. Promising findings and experimental results for the reviewed techniques suggest that OCT is an effective imaging modality for retina and retinal diseases, which can be used for early diagnosis of different diseases.

6. ACKNOWLEDGEMENT

Shlomit Schaal and Ayman El-Baz are the senior authors.

7. REFERENCES

1. D. Huang, E. Swanson, C. Lin, J. Schuman, W. Stinson, W. Chang, M. Hee, T. Flotte, K. Gregory, C. Puliafito, and J. Fujimoto: Optical coherence tomography. *Science*, 254, 1178–1181 (1991)
DOI: 10.1126/science.1957169
2. R. A. Gabbay and S. Sivarajah: Optical Coherence Tomography-Based Continuous Noninvasive Glucose Monitoring in Patients with Diabetes. *Diabetes Technol The*, 10, 188–193 (2008)
DOI: 10.1089/dia.2007.0277
3. R. V. Kuranov, J. Qiu, A. B. McElroy, A. Estrada, A. Salvaggio, J. Kiel, A. K. Dunn, T. Q. Duong, and T. E. Milner: Depth-resolved blood oxygen saturation measurement by dual-wavelength photothermal (DWP) optical coherence tomography. *Biomed Opt Express*, 2, 491–504 (2011)
DOI: 10.1364/BOE.2.000491
4. V. Kajic, B. Považay, B. Hermann, B. Hofer, D. Marshall, P. L. Rosin, and W. Drexler: Robust segmentation of intraretinal layers in the normal human fovea using a novel statistical model based on texture and shape analysis. *Opt Express*, 18, 14730–14744 (2010)
DOI: 10.1364/OE.18.014730
5. R. Kafieh, H. Rabbani, M. D. Abramoff, and M. Sonka: Intra-retinal layer segmentation of 3D optical coherence tomography using coarse grained diffusion map. *Med Image Anal*, 17, 907–928 (2013)
DOI: 10.1016/j.media.2013.05.006
6. A. Lang, A. Carass, M. Hauser, E. S. Sotirchos, P. A. Calabresi, H. S. Ying, and J. L. Prince: Retinal layer segmentation of macular OCT images using boundary classification. *Biomed Opt Express*, 4, 1133–1152 (2013)
DOI: 10.1364/BOE.4.001133
7. J. Cheng, D. Tao, Y. Quan, D. W. K. Wong, G. C. M. Cheung, M. Akiba, and J. Liu: Speckle Reduction in 3D Optical Coherence Tomography of Retina by A-Scan Reconstruction. *IEEE T Med Imaging*, 1–1 (2016)
8. W. Drexler: Optical coherence tomography: Technology and applications. *Lasers and Electro-Optics Europe (CLEO EUROPE/IQEC), Conference on and International Quantum Electronics Conference*, 1–1 (2013)
DOI: 10.1109/cleoe-iqec.2013.6802013
9. B. Potsaid, I. Gorczynska, V. J. Srinivasan, Y. Chen, J. Jiang, A. Cable, and J. G. Fujimoto: Ultrahigh speed spectral/Fourier domain OCT ophthalmic imaging at 70,000 to 312,500 axial scans per second. *Opt Express*, 16, 15149–15169 (2008)
DOI: 10.1364/OE.16.015149
10. M. E. van Velthoven, D. J. Faber, F. D. Verbraak, T. G. van Leeuwen, and M. D. de Smet: Recent developments in optical coherence tomography for imaging the retina. *Prog Retin Eye Res*, 26, 57–77 (2007)
DOI: 10.1016/j.preteyeres.2006.10.002
11. S. A. Boppart, G. J. Tearney, B. E. Bouma, J. F. Southern, M. E. Brezinski, and J. G. Fujimoto: Noninvasive assessment of the developing *Xenopus* cardiovascular system using optical coherence tomography.

- Proceedings of the National Academy of Sciences* 94, 4256–4261 (1997)
DOI: 10.1073/pnas.94.9.4256
12. M. J. Suter, S. K. Nadkarni, G. Weisz, A. Tanaka, F. A. Jaffer, B. E. Bouma, and G. J. Tearney: Intravascular optical imaging technology for investigating the coronary artery. *JACC Cardiovasc Imaging*, 4, 1022–1039 (2011)
DOI: 10.1016/j.jcmg.2011.03.020
13. G. Tearney, M. Brezinski, J. Fujimoto, N. Weissman, S. Boppart, B. Bouma, and J. Southern: Scanning single-mode fiber optic catheter–endoscope for optical coherence tomography. *Opt Lett*, 21, 543–545 (1996)
DOI: 10.1364/OL.21.000543
14. G. J. Tearney, M. E. Brezinski, B. E. Bouma, S. A. Boppart, C. Pitris, J. F. Southern, and J. G. Fujimoto: *In vivo* endoscopic optical biopsy with optical coherence tomography. *Science*, 276, 2037–2039 (1997)
DOI: 10.1126/science.276.5321.2037
15. T. Gambichler, G. Moussa, M. Sand, D. Sand, P. Altmeyer, and K. Hoffmann: Applications of optical coherence tomography in dermatology. *J Dermatol Sci*, 40, 85–94 (2005)
DOI: 10.1016/j.jdermsci.2005.07.006
16. J. Schmitt, M. Yadlowsky, and R. Bonner: Subsurface imaging of living skin with optical coherence microscopy. *Dermatology*, 191, 93–98 (1995)
DOI: 10.1159/000246523
17. K. D. Rao, Y. Verma, H. Patel, and P. Gupta: Non-invasive ophthalmic imaging of adult zebrafish eye using optical coherence tomography. *Curr Sci*, 90, 1506 (2006)
18. L. Kagemann, H. Ishikawa, J. Zou, P. Charukamnoetkanok, G. Wollstein, K. A. Townsend, M. L. Gabriele, N. Bahary, X. Wei, J. G. Fujimoto, and others: Repeated, noninvasive, high resolution spectral domain optical coherence tomography imaging of zebrafish embryos. *Mol Vis*, 14, 2157–2170 (2008)
19. S. H. Syed, K. V. Larin, M. E. Dickinson, and I. V. Larina: Optical coherence tomography for high-resolution imaging of mouse development in utero. *J Biomed Opt*, 16, 46004–46004 (2011)
DOI: 10.1117/1.3560300
20. J. C. Burton, S. Wang, C. A. Stewart, R. R. Behringer, and I. V. Larina: High-resolution three-dimensional *in vivo* imaging of mouse oviduct using optical coherence tomography. *Biomed Opt Express*, 6, 2713–2723 (2015)
DOI: 10.1364/BOE.6.002713
21. A. Alex, A. Li, X. Zeng, R. E. Tate, M. L. McKee, D. E. Capen, Z. Zhang, R. E. Tanzi, and C. Zhou: A circadian clock gene, *Cry*, affects heart morphogenesis and function in *Drosophila* as revealed by optical coherence microscopy. *PLoS One*, 10, e0137236 (2015)
DOI: 10.1371/journal.pone.0137236
22. M. Jenkins, D. Adler, M. Gargasha, R. Huber, F. Rothenberg, J. Belding, M. Watanabe, D. Wilson, J. Fujimoto, and A. Rollins: Ultrahigh-speed optical coherence tomography imaging and visualization of the embryonic avian heart using a buffered Fourier Domain Mode Locked laser. *Opt Express*, 15, 6251–6267 (2007)
DOI: 10.1364/OE.15.006251
23. A. P. Yow, J. Cheng, A. Li, C. Wall, D. W. K. Wong, J. Liu, and H. L. Tey: Skin surface topographic assessment using *in vivo* high-definition optical coherence tomography. *10th International Conference on Information, Communications and Signal Processing (ICICS)*, 1–4 (2015)
DOI: 10.1109/icics.2015.7459853
24. A. Li, J. Cheng, A. P. Yow, C. Wall, D. W. K. Wong, H. L. Tey, and J. Liu: Epidermal segmentation in high-definition optical coherence tomography. *37th Annual International Conference of the IEEE Engineering in Medicine and Biology Society (EMBC)*, 3045–3048 (2015)
25. S. S. Akhoury and L. N. Darlow: Extracting subsurface fingerprints using Optical Coherence Tomography. *Digital Information, Networking, and Wireless Communications (DINWC) Third International Conference*, 184–187 (2015)
DOI: 10.1109/dinwc.2015.7054240
26. M. W. Jenkins, M. Watanabe, and A. M. Rollins: Longitudinal Imaging of Heart Development With Optical Coherence Tomography. *IEEE J Sel Top Quantum Electron*, 18, 1166–1175 (2012)
DOI: 10.1109/JSTQE.2011.2166060

27. M. Xu, J. Cheng, D. W. K. Wong, J. Liu, A. Taruya, and A. Tanaka: Graph based lumen segmentation in optical coherence tomography images. *10th International Conference on Information, Communications and Signal Processing (ICICS)*, 1–5 (2015)
DOI: 10.1109/icics.2015.7459951
28. R. Shalev, D. Prabhu, K. Tanaka, A. M. Rollins, M. Costa, H. G. Bezerra, R. Soumya, and D. L. Wilson: Intravascular optical coherence tomography image analysis method. *41st Annual Northeast Biomedical Engineering Conference (NEBEC)*, 1–2 (2015)
DOI: 10.1109/nebec.2015.7117058
29. C. Kut, K. L. Chaichana, J. Xi, S. M. Raza, X. Ye, E. R. McVeigh, F. J. Rodriguez, A. Quiñones-Hinojosa, and X. Li: Detection of human brain cancer infiltration *ex vivo* and *in vivo* using quantitative optical coherence tomography. *Sci Transl Med*, 7, 292ra100–292ra100 (2015)
30. V. J. Srinivasan, E. T. Mandeville, A. Can, F. Blasi, M. Klimov, A. Daneshmand, J. H. Lee, E. Yu, H. Radhakrishnan, E. H. Lo, and others: Multiparametric, longitudinal optical coherence tomography imaging reveals acute injury and chronic recovery in experimental ischemic stroke. *PLoS One*, 8, e71478 (2013)
DOI: 10.1371/journal.pone.0071478
31. R. Leitgeb, M. Villiger, A. Bachmann, L. Steinmann, and T. Lasser: Extended focus depth for Fourier domain optical coherence microscopy. *Opt Lett*, 31, 2450–2452 (2006)
DOI: 10.1364/OL.31.002450
32. F. Li, T. Xu, D.-H. T. Nguyen, X. Huang, C. S. Chen, and C. Zhou: Label-free evaluation of angiogenic sprouting in microengineered devices using ultrahigh-resolution optical coherence microscopy. *J Biomed Opt*, 19, 16006–16006 (2014)
DOI: 10.1117/1.JBO.19.1.016006
33. C. Leahy, H. Radhakrishnan, and V. J. Srinivasan: Volumetric imaging and quantification of cytoarchitecture and myeloarchitecture with intrinsic scattering contrast. *Biomed Opt Express*, 4, 1978–1990 (2013)
DOI: 10.1364/BOE.4.001978
34. F. Li, Y. Song, A. Dryer, W. Cogguillo, Y. Berdichevsky, and C. Zhou: Nondestructive evaluation of progressive neuronal changes in organotypic rat hippocampal slice cultures using ultrahigh-resolution optical coherence microscopy. *Neurophotonics*, 1, 25002–25002 (2014)
DOI: 10.1117/1.NPh.1.2.025002
35. V. J. Srinivasan, H. Radhakrishnan, J. Y. Jiang, S. Barry, and A. E. Cable: Optical coherence microscopy for deep tissue imaging of the cerebral cortex with intrinsic contrast. *Opt Express*, 20, 2220–2239 (2012)
DOI: 10.1364/OE.20.002220
36. O. Assayag, K. Grieve, B. Devaux, F. Harms, J. Pallud, F. Chretien, C. Boccara, and P. Varlet: Imaging of non-tumorous and tumorous human brain tissues with full-field optical coherence tomography. *Neuroimage Clin*, 2, 549–557 (2013)
DOI: 10.1016/j.nicl.2013.04.005
37. C. Magnain, J. C. Augustinack, E. Konukoglu, M. P. Frosch, S. Sakadžić, A. Varjabedian, N. Garcia, V. J. Wedeen, D. A. Boas, and B. Fischl: Optical coherence tomography visualizes neurons in human entorhinal cortex. *Neurophotonics*, 2, 15004–15004 (2015)
DOI: 10.1117/1.NPh.2.1.015004
38. F. Shi, X. Chen, H. Zhao, W. Zhu, D. Xiang, E. Gao, M. Sonka, and H. Chen: Automated 3-D Retinal Layer Segmentation of Macular Optical Coherence Tomography Images With Serous Pigment Epithelial Detachments. *IEEE Trans Med Imaging*, 34, 441–452 (2015)
DOI: 10.1109/TMI.2014.2359980
39. J. Sugmk, S. Kiattisin, and A. Leelasantitham: Automated classification between age-related macular degeneration and Diabetic macular edema in OCT image using image segmentation. *7th Biomedical Engineering International Conference (BMEiCON)*, 1–4 (2014)
DOI: 10.1109/bmeicon.2014.7017441
40. A. Lang, A. Carass, B. M. Jodynak, S. D. Solomon, P. A. Calabresi, and J. L. Prince: Intensity inhomogeneity correction of macular OCT using N3 and retinal flatspace. *IEEE 13th International Symposium on Biomedical Imaging (ISBI)*, 197–200 (2016)
DOI: 10.1109/isbi.2016.7493243
41. J. Novosel, Z. Wang, H. de Jong, M. van Velthoven, K. A. Vermeer, and L. J. van

- Vliet: Locally-adaptive loosely-coupled level sets for retinal layer and fluid segmentation in subjects with central serous retinopathy. *IEEE 13th International Symposium on Biomedical Imaging (ISBI)*, 702–705 (2016)
DOI: 10.1109/isbi.2016.7493363
42. H. Ishikawa, D. M. Stein, G. Wollstein, S. Beaton, J. G. Fujimoto, and J. S. Schuman: Macular segmentation with optical coherence tomography. *Invest Ophthalmol Vis Sci*, 46, 2012–2017 (2005)
DOI: 10.1167/iovs.04-0335
43. M. K. Garvin, M. D. Abramoff, R. Kardon, S. R. Russell, X. Wu, and M. Sonka: Intraretinal Layer Segmentation of Macular Optical Coherence Tomography Images Using Optimal 3-D Graph Search. *IEEE Trans Med Imaging*, 27, 1495–1505 (2008)
DOI: 10.1109/TMI.2008.923966
44. A. M. Bagci, M. Shahidi, R. Ansari, M. Blair, N. P. Blair, and R. Zelkha: Thickness Profiles of Retinal Layers by Optical Coherence Tomography Image Segmentation. *AM J Ophthalmol*, 146, 679 – 687.e1 (2008)
45. S. Lu, C. Y. I. Cheung, J. Liu, J. H. Lim, C. K. s. Leung, and T. Y. Wong: Automated Layer Segmentation of Optical Coherence Tomography Images. *IEEE Trans Biomed Eng*, 57, 2605–2608 (2010)
DOI: 10.1109/TBME.2010.2055057
46. F. Rossant, I. Ghorbel, I. Bloch, M. Paques, and S. Tick: Automated segmentation of retinal layers in OCT imaging and derived ophthalmic measures. *IEEE International Symposium on Biomedical Imaging: From Nano to Macro*, 1370–1373 (2009)
DOI: 10.1109/ISBI.2009.5193320
47. Q. Yang, C. A. Reisman, Z. Wang, Y. Fukuma, M. Hangai, N. Yoshimura, A. Tomidokoro, M. Araie, A. S. Raza, D. C. Hood, and K. Chan: Automated layer segmentation of macular OCT images using dual-scale gradient information. *Opt Express*, 18, 21293–21307 (2010)
DOI: 10.1364/OE.18.021293
48. A. E. Tanboly, M. Ismail, A. Switala, M. Mahmoud, A. Soliman, T. Neyer, A. Palacio, A. Hadayer, M. El-Azab, S. Schaal, and A. El-Baz: A novel automatic segmentation of healthy and diseased retinal layers from OCT scans. *IEEE International Conference on Image Processing (ICIP)*, 116–120 (2016)
DOI: 10.1109/ICIP.2016.7532330
49. R. Brancato and B. Lumbroso: Guide to Optical Coherence Tomography Interpretation. *I.N.C Innovation-News Communication*, (2004)
50. J. S. Schuman, C. A. Puliafito, and J. G. Fujimoto: Optical Coherence Tomography of Ocular Diseases. *SLACK Incorporated*, (2004)
51. D. Koleva-Georgieva: Optical coherence tomography findings in diabetic macular edema. *INTECH Open Access Publisher*, (2012)
DOI: 10.5772/30302
52. M. Salarian, R. Ansari, J. Wanek, and M. Shahidi: Accurate segmentation of retina nerve fiber layer in OCT images. *IEEE International Conference on Electro/Information Technology (EIT)*, 653–656 (2015)
DOI: 10.1109/EIT.2015.7293411
53. S. Roychowdhury, D. D. Koozekanani, M. Reinsbach, and K. K. Parhi: 3-D localization of Diabetic Macular Edema using OCT thickness maps. *37th Annual International Conference of the IEEE Engineering in Medicine and Biology Society (EMBC)*, 4334–4337 (2015)
DOI: 10.1109/embc.2015.7319354
54. S. Lee, E. Lebed, M. V. Sarunic, and M. F. Beg: Exact Surface Registration of Retinal Surfaces From 3-D Optical Coherence Tomography Images. *IEEE Trans Biomed Eng*, 62, 609–617 (2015)
DOI: 10.1109/TBME.2014.2361778
55. H. Ishikawa, D. M. Stein, G. Wollstein, S. Beaton, J. G. Fujimoto, and J. S. Schuman: Macular Segmentation with Optical Coherence Tomography. *Invest Ophthalmol Vis Sci*, 46, 2012–2017 (2005)
DOI: 10.1167/iovs.04-0335
56. K. A. Vermeer, J. van der Schoot H. G. Lemij, and J. F. de Boer JF: Automated segmentation by pixel classification of retinal layers in ophthalmic OCT images. *Biomedical Opt Express*, 2, 1743–1756 (2011)
DOI: 10.1364/BOE.2.001743
57. H. Bogunovi, M. Sonka, Y. H. Kwon, P. Kemp, M. D. Abramoff, and X. Wu: Multi-surface and multi-field co-segmentation of 3-D retinal optical coherence tomography.

- IEEE Trans Med Imaging*, 33, 2242–2253 (2014)
DOI: 10.1109/TMI.2014.2336246
58. “American Academy of Ophthalmology Eye Wiki.” http://eyewiki.aao.org/Main_Page, (2016)
59. S.-E. Ahn, J. Oh, J.-H. Oh, I. K. Oh, S.-W. Kim, and K. Huh: Three-Dimensional Configuration of Subretinal Fluid in Central Serous Chorioretinopathy3-Dimensional Configuration of Subretinal Fluid. *Invest Ophthalmol Vis Sci*, 54, 5944–5952 (2013)
DOI: 10.1167/iov.13-12279
60. C. M. Eandi, J. E. Chung, F. Cardillo-Piccolino, and R. F. Spaide: Optical Coherence Tomography in Unilateral Resolved Central Serous Chorioretinopathy. *Retina*, 25, (2005)
DOI: 10.1097/00006982-200506000-00004
61. Y. Imamura, T. Fujiwara, R. Margolis, and R. Spaide: Enhanced Depth Imaging Optical Coherence Tomography of the Choroid in Central Serous Chorioretinopathy. *Retina*, 29, (2009)
DOI: 10.1097/IAE.0b013e3181be0a83
62. M. K. Garvin, M. D. Abramoff, X. Wu, S. R. Russell, T. L. Burns, and M. Sonka: Automated 3-D Intraretinal Layer Segmentation of Macular Spectral-Domain Optical Coherence Tomography Images. *IEEE Trans Med Imaging*, 28, 1436–1447 (2009)
DOI: 10.1109/TMI.2009.2016958
63. T. R. Hedges, L. N. Vuong, A. O. Gonzalez-Garcia, C. E. Mendoza-Santiesteban, and M. L. Amaro-Quierza: Subretinal fluid from anterior ischemic optic neuropathy demonstrated by optical coherence tomography. *Arch Ophthalmol*, 126, 812–815 (2008)
DOI: 10.1001/archoph.126.6.812
64. V. R. B. NM, D. QV, and *et al*: Prevalence of and risk factors for diabetic macular edema in the united states. *JAMA Ophthalmol*, 132, 1334–1340 (2014)
65. A. Correia, L. Pinto, A. Araújo, S. Barbeiro, F. Caramelo, P. Menezes, M. Morgado, P. Serranho, and R. Bernardes: Monte Carlo simulation of diabetic macular edema changes on optical coherence tomography data. *IEEE-EMBS International Conference on Biomedical and Health Informatics (BHI)*, 724–727 (2014)
DOI: 10.1109/BHI.2014.6864466
66. G. R. Wilkins, O. M. Houghton, and A. L. Oldenburg: Automated Segmentation of Intraretinal Cystoid Fluid in Optical Coherence Tomography. *IEEE Trans Biomed Eng*, 59, 1109–1114 (2012)
DOI: 10.1109/TBME.2012.2184759
67. S. Roychowdhury, D. D. Koozekanani, S. Radwan, and K. K. Parhi: Automated localization of cysts in diabetic macular edema using optical coherence tomography images. *35th Annual International Conference of the IEEE Engineering in Medicine and Biology Society (EMBC)*, 1426–1429 (2013)
DOI: 10.1109/embc.2013.6609778
68. A. M. Abhishek, T. T. J. M. Berendschot, S. V. Rao, and S. Dabir: Segmentation and analysis of retinal layers (ILM and RPE) in Optical Coherence Tomography images with Edema. *Biomedical Engineering and Sciences (IECBES), IEEE Conference on*, 204–209 (2014)
DOI: 10.1109/iecbes.2014.7047486
69. T. G. Rotsos and M. M. Moschos: Cystoid macular edema (2008)
70. H. Faghihi, F. Ghassemi, K. G. Falavarjani, G. S. Anari, M. Safizadeh, and K. Shahraki: Spontaneous closure of traumatic macular holes. *Can J Ophthalmol*, 49, 395–398 (2014)
71. L. Zhang, W. Zhu, F. Shi, H. Chen, and X. Chen: Automated segmentation of intraretinal cystoid macular edema for retinal 3D OCT images with macular hole. *IEEE 12th International Symposium on Biomedical Imaging (ISBI)*, 1494–1497 (2015)
DOI: 10.1109/isbi.2015.7164160
72. N. Slokom, H. Trabelsi, and I. Zghal: Segmentation of cystoids macular edema in optical coherence tomography. *2nd International Conference on Advanced Technologies for Signal and Image Processing (ATSIP)*, 303–306 (2016)
73. Q. Chen, T. Leng, L. Zheng, L. Kutzscher, J. Ma, L. de Sisternes, and D. L. Rubin: Automated drusen segmentation and quantification in SD-OCT images. *Med Image Anal*, 17, 1058–1072 (2013)
DOI: 10.1016/j.media.2013.06.003

74. P. A. Keane, P. J. Patel, S. Liakopoulos, F. M. Heussen, S. R. Sadda, and A. Tufail: Evaluation of Age-related Macular Degeneration With Optical Coherence Tomography. *Surv Ophthalmol*, 57, 389–414 (2012)
DOI: 10.1016/j.survophthal.2012.01.006
75. A. A. Khanifar, A. F. Koreishi, J. A. Izatt, and C. A. Toth: Drusen Ultrastructure Imaging with Spectral Domain Optical Coherence Tomography in Age-related Macular Degeneration. *Ophthalmology*, 115, 1883 – 1890.e1 (2008)
DOI: 10.1016/j.opththa.2008.04.041
76. S. G. Schuman, A. F. Koreishi, S. Farsiu, S. Jung, J. A. Izatt, and C. A. Toth: Photoreceptor Layer Thinning over Drusen in Eyes with Age-Related Macular Degeneration Imaged *In vivo* with Spectral-Domain Optical Coherence Tomography. *Ophthalmology*, 116, 488 – 496.e2 (2009)
DOI: 10.1016/j.opththa.2008.10.006
77. J. Oliveira, S. Pereira, L. Gonçalves, M. Ferreira, and C. A. Silva: Sparse high order potentials for extending multi-surface segmentation of OCT images with drusen. *37th Annual International Conference of the IEEE Engineering in Medicine and Biology Society (EMBC)*, 2952–2955 (2015)
DOI: 10.1109/embc.2015.7319011
78. A. Yazdanpanah, G. Hamarneh, B. Smith, and M. Sarunic: Intra-retinal layer segmentation in optical coherence tomography using an active contour approach. *International Conference on Medical Image Computing and Computer-Assisted Intervention*, 649–656 (2009)
DOI: 10.1007/978-3-642-04271-3_79
79. L. Ngo, G. Yih, S. Ji, and J. H. Han: A study on automated segmentation of retinal layers in optical coherence tomography images. *4th International Winter Conference on Brain-Computer Interface (BCI)*, 1–2 (2016)
DOI: 10.1109/iww-bci.2016.7457465
80. J. Novosel, K. A. Vermeer, L. Pierrache, C. C. W. Klaver, L. I. van den Born, and L. J. van Vliet: Method for segmentation of the layers in the outer retina. *37th Annual International Conference of the IEEE Engineering in Medicine and Biology Society (EMBC)*, 5646–5649 (2015)
DOI: 10.1109/embc.2015.7319673
81. Q. Song, J. Bai, M. K. Garvin, M. Sonka, J. M. Buatti, and X. Wu: Optimal multiple surface segmentation with shape and context priors. *IEEE Trans Med Imaging*, 32, 376–386 (2013)
DOI: 10.1109/TMI.2012.2227120
82. I. C. Han and G. J. Jaffe: Evaluation of Artifacts Associated with Macular Spectral-Domain Optical Coherence Tomography. *Ophthalmology*, 117, 1177 – 1189.e4 (2010)
DOI: 10.1016/j.opththa.2009.10.029

Abbreviations AION: Anterior Ischemic Optic Neuropathy, AMD: age-related macular degeneration (AMD), BM: Bruch's Membrane, CAD: computer aided diagnosis, CME: Cystoids macular edema, CSC: central serous chorioretinopathy, DME: diabetic macular edema, ELM: External limiting membrane, GCL: Ganglion Cell Layer, ILM: Inner Limiting Membrane, INL: Inner Nuclear Layer, IPL: Inner Plexiform Layer, IRC: inner retinal complex, NFL: Nerve Fiber Layer, NION: non-arteritic AION, OCT: optical coherence tomography, ONL: Outer Nuclear Layer, OPL: Outer Plexiform Layer, ORB: Outer Photoreceptor, ORC: outer retinal complex, PED: retinal pigment epithelial detachments, PIS: Photoreceptor Inner Segments, POS: Photoreceptor Outer Segments, RPE: retinal pigment epithelium, SD-OCT: spectral-domain optical coherence tomography, TD-OCT: time-domain optical coherence tomography

Key Words Optical coherence tomography, OCT images, Diagnosing retinal diseases, Retina anatomy in OCT, Glaucoma, Central serous chorioretinopathy, CSC, Unilateral anterior ischemic optical neuropathy, AION, Diabetic macular edema, DME, Cystoids macular edema, CME, Age-related macular degeneration, AMD, Review

Send correspondence to: Ayman El-Baz, Bioengineering Department, University of Louisville, Louisville, KY, USA, Tel: 502-852-5092, Fax: 502-852-1577, E-mail: aselba01@louisville.edu